Journal of Alloys and Compounds 834 (2020) 155077

Contents lists available at ScienceDirect

Journal of Alloys and Compounds

journal homepage: http://www.elsevier.com/locate/jalcom

Multi-microalloying mediated grain growth and texture evolution during the high-temperature static recrystallization of AZ80 alloys

Lingbao Ren [a, b, *], Mingyang Zhou [c], Carl J. Boehlert [d], Gaofeng Quan [c, **]

[a] Shaanxi Key Laboratory of Low Metamorphic Coal Clean Utilization, School of Chemistry and Chemical Engineering, Yulin University, Yulin, 719000, PR China
[b] Center for Advancing Materials Performance from the Nanoscale, State Key Laboratory for Mechanical Behavior of Materials, Xi'an Jiaotong University, Xi'an, 710049, PR China
[c] School of Materials Science and Engineering, Southwest Jiaotong University, Chengdu, 610031, PR China
[d] Department of Chemical Engineering and Materials Science, Michigan State University, East Lansing, MI, 48824, USA

ARTICLE INFO

Article history:
Received 5 October 2019
Received in revised form
15 March 2020
Accepted 5 April 2020
Available online 10 April 2020

Keywords:
Microalloying
Grain growth
Texture
Magnesium
Rare earth
Hardness

ABSTRACT

Y, (Y + Nd), and (Y + Ca) multi-microalloying, which has potential to mediate the grain growth and texture evolution, played an important role in the mechanical properties of the studied extruded AZ80 sheet. Quasi-in-situ electron backscattered diffraction results revealed that grain boundary migration and grain rotation simultaneously occurred during the grain growth. All these three microalloying combinations effectively lowered the grain growth rate. In particular, the AZ80 + 0.2Y+0.15Ca maintained the lowest growth rate and the most uniform fine grain structure. The rare-earth (RE) texture components, which temporarily formed in AZ80 + 0.2Y and AZ80 + 0.1Y+0.1Nd, weakened their basal texture intensity. In contrast, continuously enhanced basal texture, accompanied by grain growth, dominated the texture evolution in AZ80 + 0.2Y+0.15Ca. As a result, all microalloyed combinations exhibited lower Vickers hardness than that of AZ80. The microalloying also reduced the hardness anisotropy of the sheets.

© 2020 Elsevier B.V. All rights reserved.

1. Introduction

Alloying is often performed to modify the microstructure and mechanical properties of magnesium (Mg) alloys. For example, heavy RE additions, such as yttrium (Y), gadolinium (Gd), have contributed to high strength (tensile strength: 417–542 MPa) Mg alloys (e.g., Mg-3.9Zn-1.6Gd [1], Mg-10Gd-5.7Y-1.6Zn-0.6Zr [2]). However, such Mg alloys are expensive and lead to risks associated with progressive resource exhaustion and unavailability of critical elements [3,4]. Therefore, low-cost Mg alloys, containing either low RE content or no RE elements, should be appropriately considered in the materials design.

For example, 0.03 wt% Nd addition makes pearlite denser and increases the hardness of Fe-0.66C-0.67Mn-0.20Si (wt.%) alloys [5]. For Mg–Al based alloys, more than 14 elements have been studied to reveal the effects of microalloying on the microstructure and mechanical properties [6–12]. Table 1 briefly summarizes the mechanical properties (UTS, YS, and ε_f) of some microalloyed Mg–Al based alloys. Trace alloying additions (e.g., Ca, Sr, Y, La, Gd < 0.5 wt%) to Mg–Al alloys significantly refine the eutectic β-$Mg_{17}Al_{12}$ phase and change its volume fraction [7–13]. Appropriate microalloying can improve the strength by either refining the grain size or stabilizing disperse, fine secondary phases. However, an excess of elemental additions will result in a degradation of the mechanical properties, which has been observed in Mg–4Al–4La+0.5Sr (wt.%) or AZ80 + 0.8Y (wt.%) [6,12]. An example of appropriate alloying addition is (Y + Ca) dual microalloying (<0.5 wt%), which effectively increased the AZ80 ignition temperature to about 820 °C (for a 0.1 g chip) resulting from the double-layered structure of $CaO + Y_2O_3$ and $MgO + CaO + Al_2O_3$ on the molten surface [11].

Solute segregation at the interfaces (grain boundary (GB), twin boundary, etc.) plays an important role in the interface mobility by accommodating the interface energy and the solute drag force [14]. For example, the periodic segregation of Gd or (Nd + Ag) atoms at

* Corresponding author. Shaanxi Key Laboratory of Low Metamorphic Coal Clean Utilization, School of Chemistry and Chemical Engineering, Yulin University, Yulin, 719000, PR China.
** Corresponding author.
E-mail addresses: renlingbao@xjtu.edu.cn (L. Ren), quangf@swjtu.edu.cn (G. Quan).

https://doi.org/10.1016/j.jallcom.2020.155077
0925-8388/© 2020 Elsevier B.V. All rights reserved.

Table 1
Mechanical properties (UTS, YS, and ε_f) of microalloyed Mg–Al alloys after different processing conditions.

Alloy (wt.%)	Processing condition	Grain size (μm)	f (β-$Mg_{17}Al_{12}$) (vol%)	UTS (MPa)	YS (MPa)	ε_f (%)	Ref.
Mg–4Al–4La	As-cast	–	–	224	148	7	[6]
Mg–4Al–4La (0.25Sr)	As-cast	–	–	254	160	10	[6]
Mg–4Al–4La (0.50Sr)	As-cast	–	–	240	155	7	[6]
Mg–4Al-0.3Mn	Extruded (350 °C)	15	–	282	198	9	[7]
Mg–4Al-0.3Mn (1.0Y)	Extruded (350 °C)	9	–	293	212	8	[7]
AZ61	As-cast + T4	150	11*	190	120	4	[8]
AZ61 (1.0Sm)	As-cast + T4	100	7*	220	140	4	[8]
AZ80	As-cast	350	8	170	65	6	[9]
AZ80 (0.2Y)	As-cast	410	14	230	70	10	[9]
AZ80 (0.8Y)	As-cast	420	16	210	60	11	[9]
AZ80	Extruded (230 °C)	2	7	362	282	14	[10]
AZ80 (1.07La+0.52Gd)	Extruded (230 °C)	1	13	397	341	11	[10]
AZ80 (0.2Y+0.3Ca)	LTSS Extruded (200 °C)	–	1	421	380	11	[11]
AZ80	Extruded (350 °C)	9	10	340	160	13	[12]
AZ80 (0.8Y)	Extruded (350 °C)	40	1	348	127	18	[12]

All the properties listed were from tensile tests performed at a strain rate of $10^{-3}s^{-1}$; *Volume percent of the β; T4: 420 °C/24 h solution treatment; LTSS: Low-temperature-slow-speed extrusion.

twin boundaries during annealing leads to enhanced stability (low mobility) of the twin boundary (TB) [14,15]. Besides, the GB segregation of Y or Ca, revealed through HAADF-STEM observations [16,17], generates a significant drag effect and retards both grain growth and GB migration. It has also been reported that co-segregation (e.g., Ca + Zn) improves GB stability during static recrystallization [18]. This microalloying-elements-segregation enhanced stability in TB or GB resulted in additional strengthening [15] and suppression of abnormal dynamic recrystallization grain growth during high-speed extrusion.

Stanford et al. [19] reported that RE addition can effectively weaken the texture intensity due to the appearance of a new texture component (termed "RE texture") during extrusion, in which the peak texture intensity reduced and the <0001> poles tilted toward the transverse direction (TD) after subsequent annealing [20,21]. The concentration of the Y and Nd required for texture weakening of binary Mg-RE alloys was less than 0.7 wt%, and 0.2 wt%, respectively [22], which implies that microalloying has potential to modify the texture. Barrett et al. [23] indicated that Y segregation at the GB homogenizes the GB energy and mobility. The migration of some special boundaries is deterred thereby allowing other orientations to thrive before grain growth saturates, which results in a less intense texture than that typically observed in RE containing Mg alloys. Thus, trace additions of RE elements might be an effective approach to modify the crystallographic texture during extrusion, leading to an increase in ε_f. Furthermore, trace Ca addition can both relieve the misfit strain near precipitates and reduce the energy barrier for precipitate nucleation [24].

As mentioned above, both the high-solubility (12.5 wt%) element, Y, and two low-solubility (<3.6 wt%) elements, Nd and Ca, have a significant effect on the GB migration and texture evolution. However, there was little knowledge to clarify the tailoring effect of these alloying elements on the static recrystallization of AZ80. In this work, we first added Y, (Y+Nd) and (Y+Ca) in AZ80 to estimate the microalloying effect on the grain growth kinetics during long term (~480 h) annealing; Second, the texture evolution was elucidated; Third, we measured the hardness anisotropy sensitivity. This will give insight into developing a low-cost tailoring methods (e.g., grain size refinement and texture weakening) for high-performance extruded AZ80 alloys.

2. Materials and experimental procedures

2.1. Materials and processing

Four Mg–8Al-0.5Zn based alloys were studied (see Table 2). The alloys were prepared by resistance melting pure Mg (99.9 wt%), pure Al (99.9 wt%), pure Zn (99.9 wt%), Mg–30Y (wt.%), Mg–30Nd (wt.%) and Mg–25Ca (wt.%) master alloys. The molten Mg was protected from oxidation by a covering flux and CO_2+2 vol% SF_6 mixed gas. The melt was held at 740 °C for 50–60 min, then poured into a steel die of 95 mm diameter. The homogenization annealing for these billets was conducted at 420 °C for 8 h, followed by air cooling. The billets were then machined into 88 mm diameter round bars. Before extrusion, the billets were preheated at 350 °C for 3–4 h. The extrusion container and the extrusion die were preheated to 300 °C and 400 °C, respectively. Subsequently, the billets were extruded to 80 mm × 5 mm sheets with a 16:1 extrusion ratio and a 0.5–1.0 mm/s ram speed.

Table 2
Nominal chemical compositions of the AZ80 and microalloyed AZ80 alloys (wt.%).

Alloy	Al	Zn	Mn	Y	Nd	Ca	Mg
AZ80	8.0	0.5	0.2	–	–	–	Bal.
AZ80+0.2Y	8.0	0.5	0.2	0.2	–	–	Bal.
AZ80+0.1Y+0.1Nd	8.0	0.5	0.2	0.1	0.1	–	Bal.
AZ80+0.2Y+0.15Ca	8.0	0.5	0.2	0.2	–	0.15	Bal.

2.2. Annealing heat treatments

Rectangular plates 12 (ED) × 8 (TD) × 4 (ND) mm^3 were cut from the center of the as-extruded sheets using electrical discharge machining (where ED, TD, and ND represent the extrusion direction, transverse direction, and normal direction, respectively[1]). The samples were first ground using silicon carbide (SiC) papers through 400, 800, and 1200 grits (US standards) to remove the surface damage and pollution, followed by ultrasonic bath cleaning with ethanol. For the 420 °C/4 h and 420 °C/7 h annealing treatments, the cleaned samples were put in the middle of a quartz glass tube, and a thermocouple was welded along the sample thickness to monitor the temperature. The glass tube was evacuated using a mechanical pump for about 10 min to minimize thick oxidation during the annealing treatment. The sealed quartz glass tube was put in a tube furnace and heated to 420 °C, then held for either 4 h or 7 h. The glass tube was then taken out of the furnace, and the sample was cooled to less than 50 °C using compressed air (20 psi). The long term (410 °C/480 h) annealing treatment was conducted

[1] The sample coordinate system was constant throughout this paper.

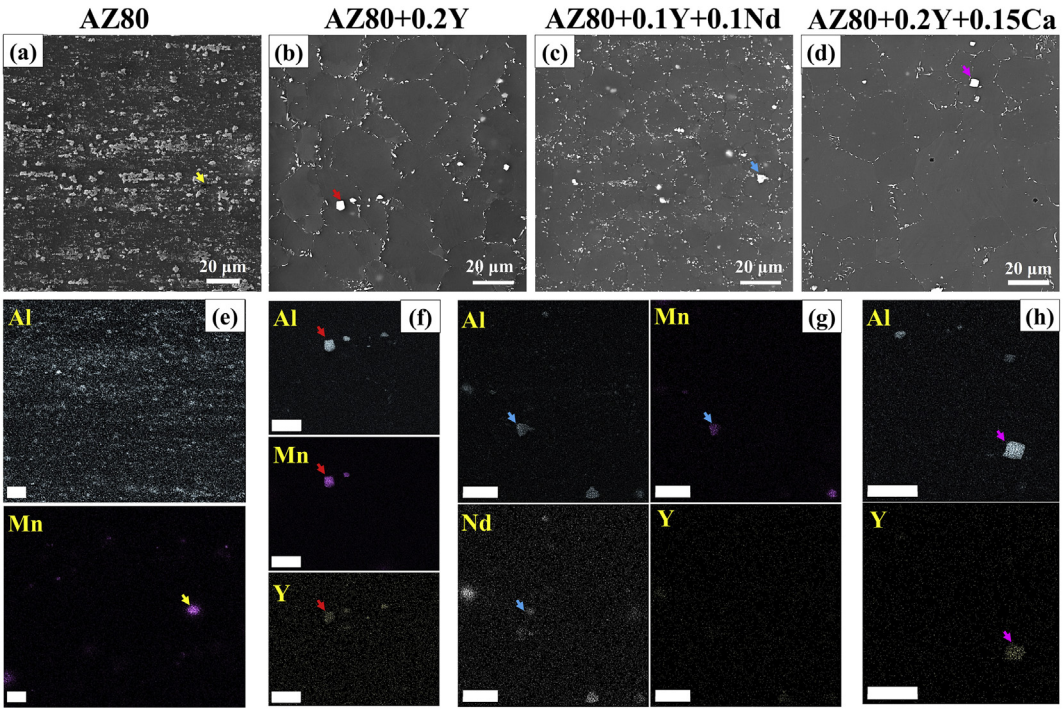

Fig. 1. (a–d) Secondary electron SEM photomicrographs for as-extruded AZ80, AZ80 + 0.2Y, AZ80 + 0.1Y+0.1Nd, and AZ80 + 0.2Y+0.15Ca sheets in the ND plane, respectively. (e–h) Energy dispersive spectroscopy (EDS) map for the as-extruded sheets in the ND plane, respectively, and the arrows in the EDS maps highlighting the intermetallic compounds in (a–d). All EDS maps have scale bars of 10 μm in (e–h).

in a creep furnace. The samples were then cooled in air and ground to less than 3 mm thickness to avoid characterizing the oxide-influenced surface.

2.3. Microstructure characterization and hardness test

The microstructure of the alloys was observed using a Nikon 120C optical microscope (OM) and a TESCAN MIRA III FEG scanning electron microscope (SEM) equipped with an energy dispersive spectroscopy (EDS) system. The average grain size was estimated by the line intercept method (GB/T 6394–2017) and the phase volume percents were measured by the grid point method. The EDAX-TSL electron backscattered diffraction (EBSD) system was used to identify the grain orientation and texture features on the ND plane containing at least 1000 grains. The scanning step size was 0.2–0.4 μm/step and data post-processing was performed using EDAX OIM Analysis 7 software. The SEM accelerating voltage was 30 kV, and the working distance was 16 mm. Metallographic samples were ground using SiC planar grinding papers through 400, 800, 1200 grits, respectively. The samples were then polished through 1.0 μm, 0.25 μm diamond pastes, and 0.04 μm colloidal silica solution was used for the final polishing. The samples were etched using a solution containing 60 ml ethanol, 20 ml water, 15 ml acetic acid, and 5 ml nitric acid. The phase compositions were identified using a Bruker D2 PHASER X-ray diffraction (XRD) system in the sample's ND plane, and the scanning speed was 0.05°/step with 2θ ranging between 20 and 90°. Room-temperature hardness tests were conducted using a LECO M-400-G1 microhardness tester with 500 g load and 10 s dwell time. 5 indents tests were performed on the mechanically polished ND plane and the results were averaged.

3. Results and discussion

3.1. As-extruded microstructure

Fig. 1 shows the microstructure of the as-extruded sheets in ND. As Fig. (a–d) shown, the grain size of the microalloyed AZ80 sheets was larger than that of AZ80. AZ80 + 0.1Y+0.1Nd exhibited a finer grain size than that of the AZ80 + 0.2Y and AZ80 + 0.2Y+0.15Ca. The average diameter of the GB precipitates in AZ80 + 0.1Y+0.1Nd (0.8 ± 0.2 μm) was less than that of AZ80 + 0.2Y (1.8 ± 0.5 μm) and AZ80 + 0.2Y+0.15Ca (2.2 ± 0.6 μm). The GB precipitate volume percents in AZ80, AZ80 + 0.2Y, AZ80 + 0.1Y+0.1Nd, and AZ80 + 0.2Y+0.15Ca were 27 %, 6 %, 12 %, and 5 %, respectively. Less than 1 vol% of the polygonal particles was distributed at the GBs and grain interiors of the alloys.

First-principles calculations revealed that the Al_2Y, $(Mg,Al)_2Ca$ and Al_2Nd Laves phase have the low enthalpies of formation in Mg–Al–Y, Mg–Al–Ca or Mg–Al-Nd system, respectively, which thermodynamically favor the formation of these stable intermetallic compounds [25–29]. Fig. 1(e–h) present the EDS results for as-extruded AZ80, AZ80 + 0.2Y, AZ80 + 0.1Y+0.1Nd, and AZ80 + 0.2Y+0.15Ca, respectively. Al and Mn-rich particles were observed in all studied alloys, and Y or Nd containing compounds were also detected in the corresponding alloys (Fig. 1(g–h)).

3.2. Grain growth kinetics and GB migration

Fig. 2 provides a comparison between the as-extruded and 420 °C/7 h annealed microstructures. Fig. 2(e–f) shows that the annealed AZ80 and AZ80 + 0.2Y exhibited larger grain sizes than that of AZ80 + 0.1Y+0.1Nd and AZ80 + 0.2Y+0.15Ca. For example, the grain size of AZ80 + 0.2Y+0.15Ca increased from 32 ± 3 μm to 52 ± 3 μm while the grain size of AZ80 + 0.2Y increased from 32 ± 3 μm to 96 ± 13 μm (see Table 3). The recrystallization kinetics

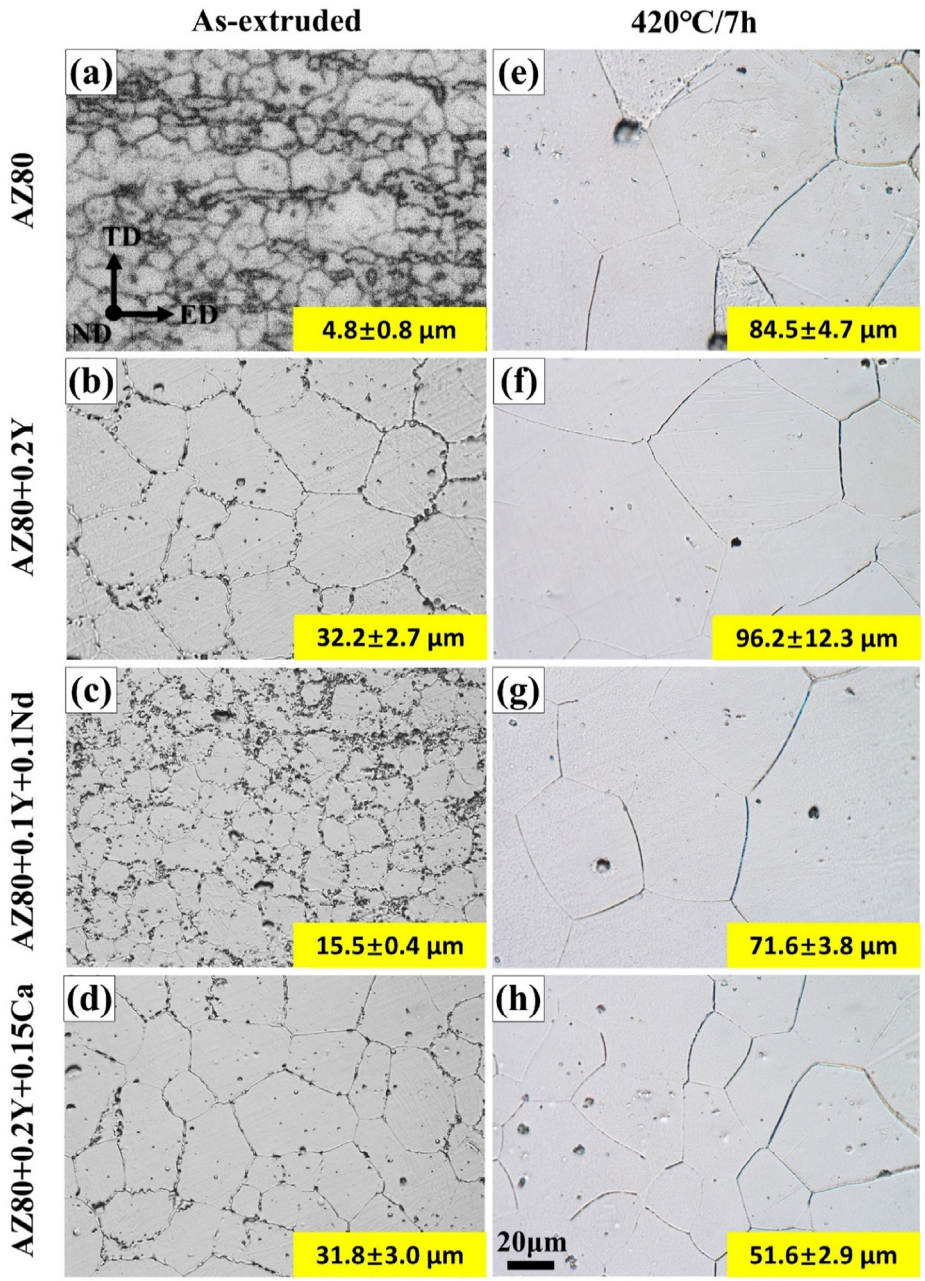

Fig. 2. (a–d) Optical photomicrographs for extruded AZ80 + 0.2Y, AZ80 + 0.1Y+0.1Nd, and AZ80 + 0.2Y+0.15Ca sheets in the ND plane. (e–h) Optical photomicrographs for the 420 °C/7 h annealed samples in the ND plane. The average grain size values are labeled in yellow for each condition. (For interpretation of the references to colour in this figure legend, the reader is referred to the Web version of this article.)

Table 3
The average grain size after different processing conditions (μm).

Alloy	As-extruded	420 °C/4 h annealing	420 °C/7 h annealing	410 °C/480 h annealing
AZ80	5±1	65±2	84±5	>2000
AZ80+0.2Y	32±3	79 ±5	96±13	184±65
AZ80+0.1Y+0.1Nd	15±1	57±5	72±5	112±42
AZ80+0.2Y+0.15Ca	32±3	40±1	52±3	–

were analyzed based on Eq. (1) [30], where d is the annealed grain size, μm; d_0 is the as-extruded grain size, μm; t is the annealing time, h; and n is the grain growth exponent. The constant, k, varies with temperature according to the relationship described in Eq. (2), where R and k_0 are constant, T is annealing temperature, and Q_G is the activation energy for grain growth. It was found that $n = 2$ provided a good fit for the grain growth behavior (see Fig. 3).

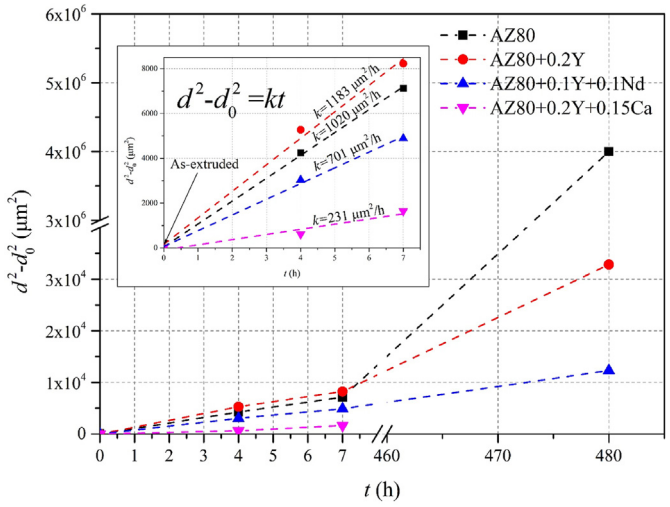

Fig. 3. d^2-d_0^2 value as a function of the annealing time for different alloys. d and d_0 are the average grain size of the annealed and as-extruded samples, respectively; t is the annealing time; short time (0–7 h) conditions are presented in the inset.

$$d^n - d_0^n = kt \quad (1)$$

$$k = k_0 \exp(-Q_G / RT) \quad (2)$$

The average grain growth velocity ($\Delta(d^2 - d_0^2)/\Delta t$) for the 420 °C/7 h annealing treatment was labeled in the inset of Fig. 3. The greatest velocity was observed in AZ80 + 0.2Y, followed by AZ80, AZ80 + 0.1Y+0.1Nd, and AZ80 + 0.2Y+0.15Ca. The (Y + Ca) alloy exhibited the greatest grain growth suppression and exhibited a growth velocity of 231 μm²/h which was less than one quarter that of the AZ80 (1020 μm²/h) and AZ80 + 0.2Y (1183 μm²/h). For the 410 °C/480 h annealing treatment, AZ80 exhibited the largest average grain size (>2000 μm), which was more than ten times that of AZ80 + 0.2Y (184 μm) and AZ80 + 0.1Y+0.1Nd (112 μm) (see Table 3).

Assuming that the boundary migration rate is equal to the grain growth rate, we can show that [31]:

$$V_{GB} = (D_{GB}\Omega / kT\delta_{GB})\gamma_{GB}(\alpha / d) \quad (3)$$

where V_{GB} is the GB migration velocity, D_{GB} corresponds to a diffusion coefficient through the GB for all solutes, Ω is the atomic volume through the GB, δ_{GB} is the thickness of the GBs, γ_{GB} is the GB energy, α is a proportionality constant dependent on the grain shape, and d is the grain diameter.

The microalloying elements (Y, Nd, Ca) segregation into the GB influenced the GB mobility and thus the grain growth kinetics [18,23]. Barrett et al. [23] reported that Y segregation at the GB greatly reduced γ_{GB}, and thus a small percentage of Y addition can homogenize the energy and mobility of GBs, resulting in a less intense texture. The texture evolution will be discussed in section 3.3. The presence of Ca atoms next to Y atoms reduces the basal plane strain imposed on the Mg matrix [32]. Thus, according to Eq. (3), the co-segregation of Ca and Y may further reduce the γ_{GB} and decrease the GB mobility, which is consistent with the experimental results shown in Fig. 3. As stated above, the grain size for the

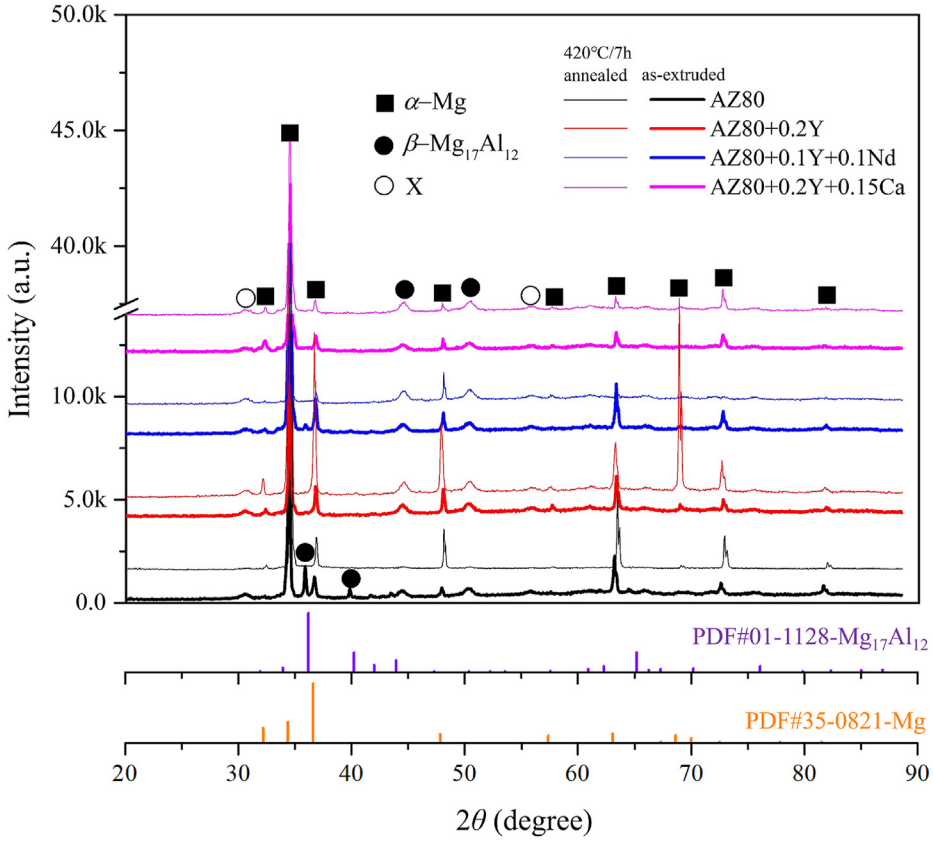

Fig. 4. X-ray diffraction (XRD) patterns for the as-extruded and 420 °C/7 h annealed alloys in the ED-TD plane. "X" represents unidentified peaks. The PDF compounds phase information is referenced on the bottom.

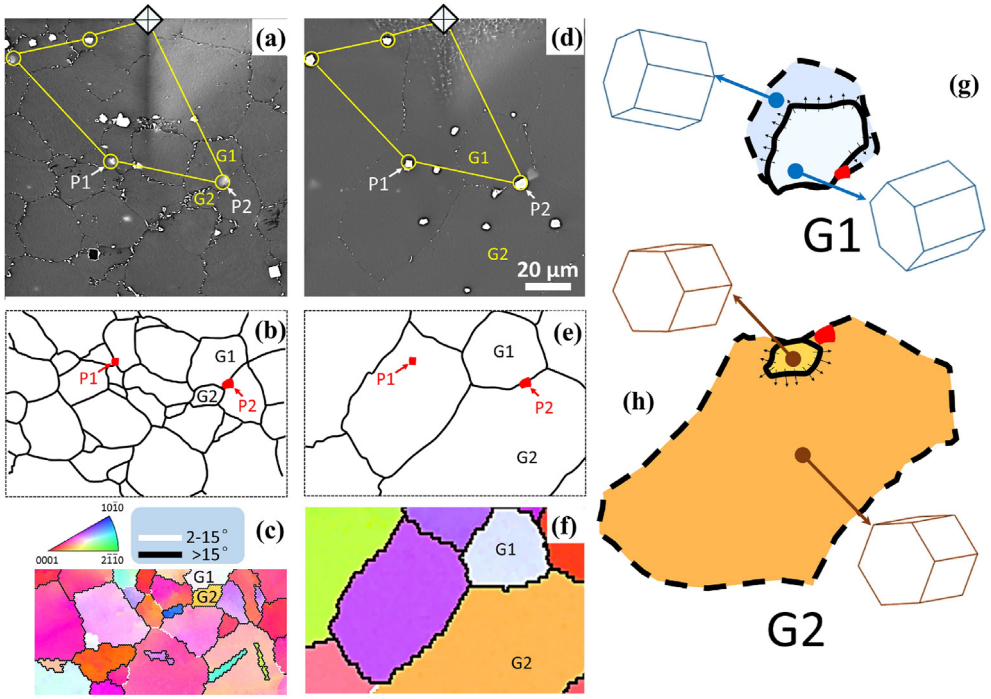

Fig. 5. Quasi-in-situ SE SEM photomicrographs of the (a) as-extruded AZ80 + 0.2Y; (d) after 420 °C/4 h annealing. (b, c) and (e, f) Corresponding grain boundary images and EBSD orientation maps for (a, d), respectively. (g, h) Grain boundary migration in grain G1 and G2, respectively.

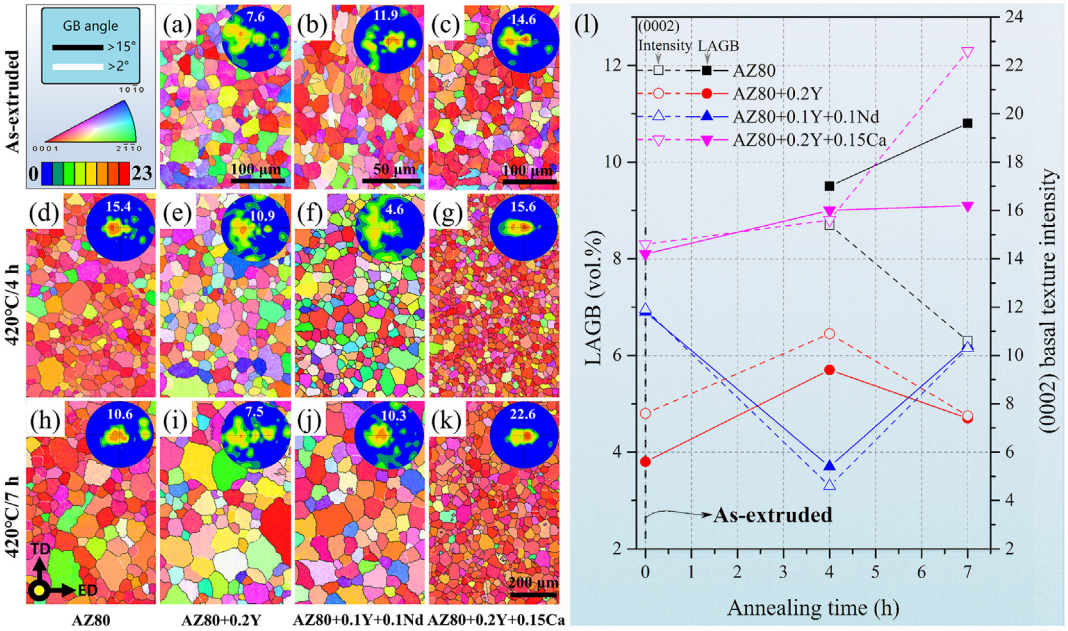

Fig. 6. EBSD orientation maps in (a–c) as-extruded, (d–g) 420 °C/4 h, and (h–k) 420 °C/7 h conditions in the ED-TD plane. The (d–k) annealed EBSD maps have the same scale bar. The white and black lines represent the low-angle (2–15°) grain boundaries (LAGB) and high-angle (>15°) grain boundaries, respectively; (0002) pole figures and the maximum intensity values are provided in the insert of the corresponding EBSD maps; (l) LAGB and the (0002) basal texture maximum intensity as a function of the annealing time.

AZ80 + 0.2Y+0.15Ca was indeed smaller than those in the two counterpart alloys (AZ80 + 0.2Y, AZ80 + 0.1Y+0.1Nd) at each stage of recrystallization, and the grain size distribution in the AZ80 + 0.2Y+0.15Ca alloy was significantly narrower than those for the two counterpart alloys, see Table 3. This was attributed to the decreasing GB energy and increasing solute drag effect resulting from the co-segregation of Ca and Y. This led to a more uniform growth of the recrystallized grains.

On the other hand, the grain growth during annealing led to a decrease of the GB density (ρ_{GB}, grain boundary area per unit volume). For grains assumed to be spherical with a diameter d, the GB density can be written as [31]:

$$\rho_{GB} = [4\pi \times (d/2)^2]/\,[2 \times 4\pi/3 \times (d/2)^3] = 3/d \quad (4)$$

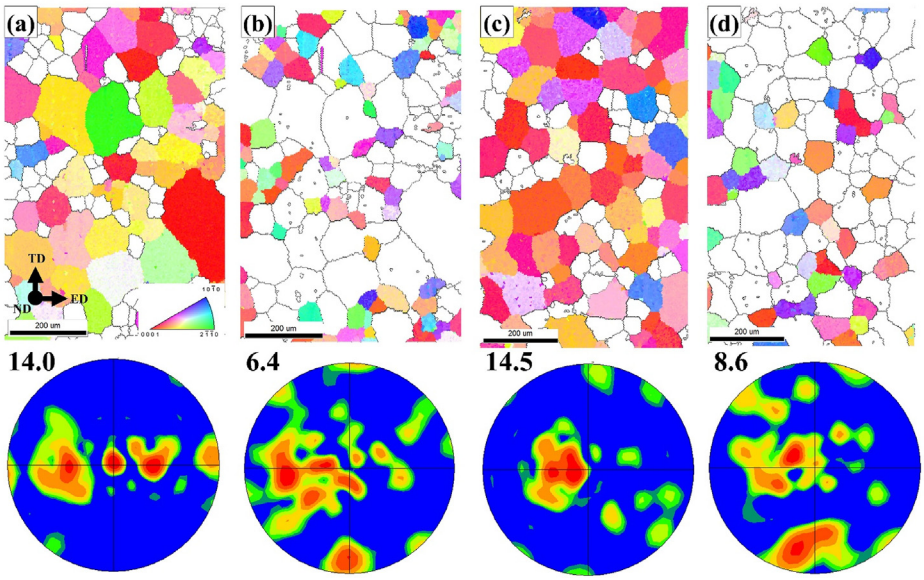

Fig. 7. EBSD orientation maps and (0002) pole figures showing the grains whose size are (a, c) larger or (b, d) smaller than the average grain size in 420 °C/7 h annealed (a, b) AZ80 + 0.2Y, and (c, d) AZ80 + 0.1Y+0.1Nd.

Thus, the GB solute concentration increases with grain growth according to:

$$C{=}Cv + C_{GB}\rho_{GB} = C_V + C_{GB}(3/d) \quad (5)$$

where C, Cv, and C_{GB} are the solute concentrations in the whole material, in the grains, and at the GBs, respectively. Increasing GB solute concentration further enhances the drag force for the GB migration and retards the grain growth. This is consistent with the annealing results, especially for the long-term annealing conditions. For example, the grain size of the microalloyed AZ80 is less than one-tenth of that of AZ80 after 410 °C/480 h annealing (Table 3), which demonstrates that increasing the Y or (Y + Nd) concentration at the GB dramatically retards the grain growth.

The comparison of the XRD patterns for the as-extruded and 420 °C/7 h annealed microstructures is presented in Fig. 4. For the as-extruded sheets, β-$Mg_{17}Al_{12}$ peaks were prevalent in the AZ80, and AZ80 + 0.1Y+0.1Nd alloys, while they were rarely observed in AZ80 + 0.2Y and AZ80 + 0.2Y+0.15Ca. After the 420 °C/7 h annealing treatment, the β-$Mg_{17}Al_{12}$ peaks were not evident. However, the undetermined phase peaks, X (highlighted by circles), were stable in the alloys after annealing, and they disappeared in the annealed AZ80.

The grain growth was investigated using EBSD in the MMA AZ80 alloys. Here we take AZ80 + 0.2Y as a model alloy to quasi-in-situ reveal the process of GB migration as well as grain rotation during annealing. The corresponding SEM map, GB map and EBSD orientation map of the in-situ region prior to annealing are presented in Fig. 5(a-c), respectively. Four Al_2Y particles and the indentation center composed a constellation-like marker to help reference the in-situ EBSD test region. Twins were distinguished in as-extruded EBSD map (see Fig. 5 (c)). Fig. 5 (d) shows the 420 °C/4 h annealed microstructure of AZ80 + 0.2Y. The constellation-like markers were stable: "P1" Al_2Y particle was enwrapped in the grown grain, while "P2" remained at a GB (see Fig. 5(e)). The interaction between the A_2Y particles and the GB migration above implies that the resistance of the micron-size intergranular Al_2Y to GB migration is poor. Tracking the "G1", "G2" grain evolution throughout the annealing, it is suggested that grain growth and grain rotation occurred concurrently during the static recrystallization (SRX). Grain rotation is prevalent in the plastic deformation of polycrystalline metals, which contributes to the change of the average spacing of the GB dislocations [33]. The grain maps in Fig. 5(g–h) indicate that grain rotation occurred in the "G1" grain accompanied with GB migration, while the "G2" grain exhibited less rotation. Thus, diffusion at the GB may result in a change of the dislocation spacing with GB migration.

3.3. Texture evolution during the static recrystallization

Texture serves as another key microstructural variable to tailor the mechanical properties of the extruded profile and thus the microalloying effect on texture variation accompanied by grain growth need to be clarified as well. Fig. 6 shows EBSD orientation maps for the as-extruded and annealed alloys and the corresponding (0002) pole figures (PFs), which are consistent with the SEM and OM results in Figs. 1 and 2. The maximum (0002) texture intensity was labeled in each EBSD orientation map as well. In Fig. 6(a and b), the <0001> poles in the PFs of the as-extruded AZ80 + 0.2Y and AZ80 + 0.1Y+0.1Nd tilted away from ND and extended toward the TD, which represents a typical RE texture. After 420 °C/4 h annealing, Fig. 6(e and f) show additional <0001> poles tilted toward TD for AZ80 + 0.2Y and AZ80 + 0.1Y+0.1Nd, and the enhanced RE texture in AZ80 + 0.1Y+0.1Nd resulted in a large decrease in texture intensity, which is consistent with a previous report [20,21]. When the annealing duration was extended to 7 h (Fig. 6(i and j)), the RE texture in AZ80 + 0.2Y became weaker and more <0001> poles tilted toward ED. Less <0001> poles tilted toward TD for AZ80 + 0.1Y+0.1Nd, and a higher maximum texture intensity was observed. For AZ80 + 0.2Y+0.15Ca EBSD orientation maps (Fig. 6 (c, g, k)), the as-extruded and 420 °C/4 h annealed PFs show two separated <0001> pole peaks situated away from the center of the PF and toward the ED. This split of the <0001> pole peaks became inconspicuous after 420 °C/7 h annealing. (Y + Ca) addition resulted in a very different texture evolution compared with only Y addition. The basal texture intensity was continuously strengthened from 14.6 to 22.6 with increased annealing time, which was also found in rolled AZ31 [34]. Fig. 6 (d, h) shows that all

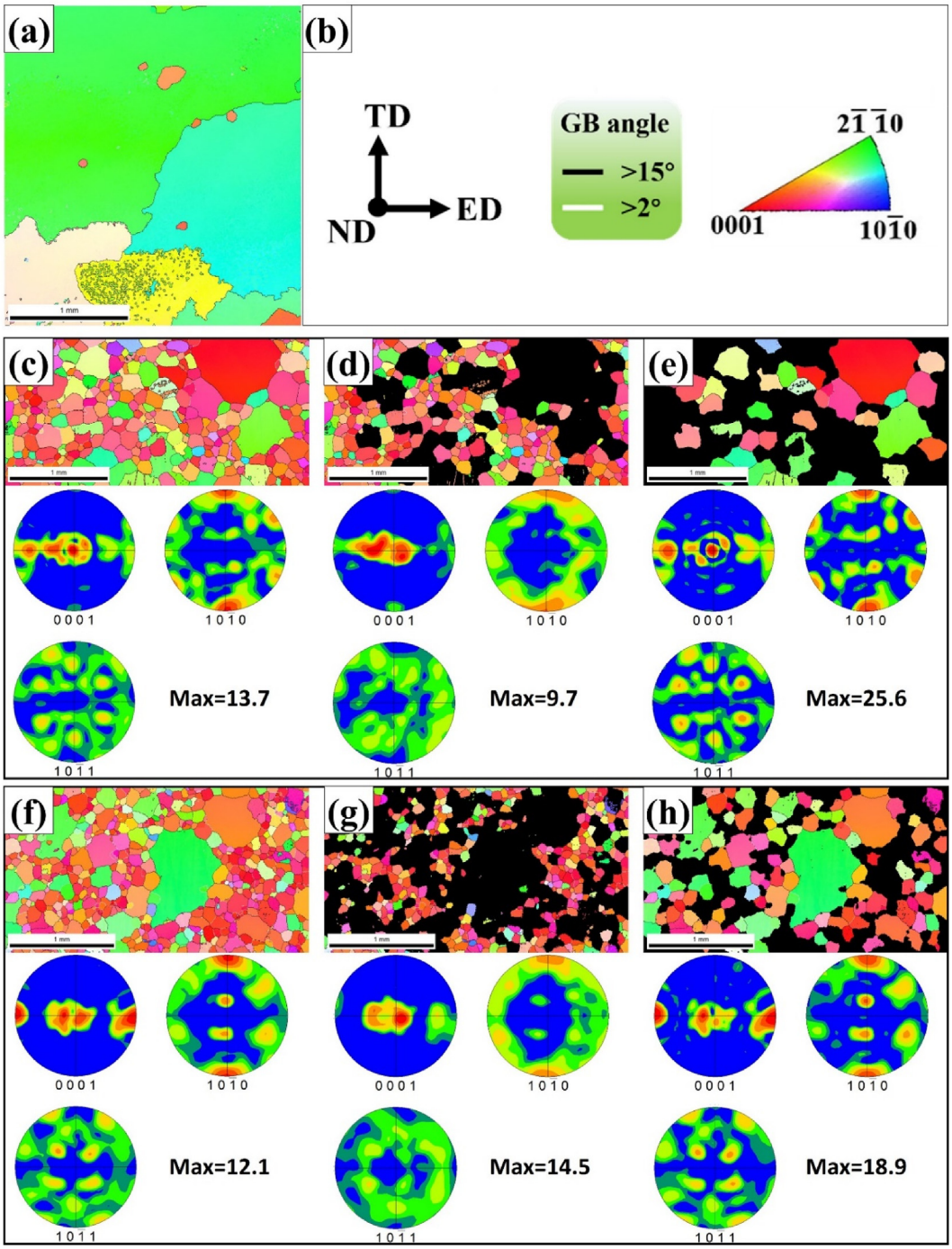

Fig. 8. EBSD orientation maps of 410 °C/480 h annealed (a) AZ80, (c–e) AZ80 + 0.2Y, and (f–h) AZ80 + 0.1Y+0.1Nd, where the white and black lines represent the low-angle (2–15°) grain boundaries (LAGB) and high-angle (>15°) grain boundaries, respectively; (d) and (e) are EBSD orientation maps of the smaller grains (<183 μm) and larger grains (>183 μm) represented in (c), respectively; (g) and (h) are EBSD orientation maps of the smaller grains (<112 μm) and larger grains (>112 μm) represented in (f), respectively; (0001), (10-10), and (10–11) pole figures and the maximum texture intensity are provided under the corresponding EBSD orientation maps; (b) indicated the sample coordinate system, grain boundary angle classification, and the inverse pole figure, respectively.

annealed AZ80 base alloys exhibited a basal texture and maintained higher texture intensity than the Y and (Y + Nd) microalloyed alloys.

Fig. 6 (l) briefly summaries the volume percent of the low angle grain boundaries (LAGBs) and the (0002) basal texture intensity as functions of the annealing time for the studied alloys. For the as-extruded conditions, AZ80 + 0.1Y+0.1Nd and AZ80 + 0.2Y+0.15Ca exhibited higher LAGB volume percent than AZ80 + 0.2Y, which had lower grain growth kinetics (see Fig. 3). AZ80 and AZ80 + 0.2Y+0.15Ca maintained higher LAGB volume percent for both as-extruded and annealed conditions. Besides, the variation trend was similar between LAGB volume percent and (0002) basal texture intensity in the ND plane of the microalloyed sheets indicating that the <0001> pole of the grain pair containing LAGB possibly preferred to align along the ND direction, while the AZ80 didn't follow this pattern. As discussed above, the

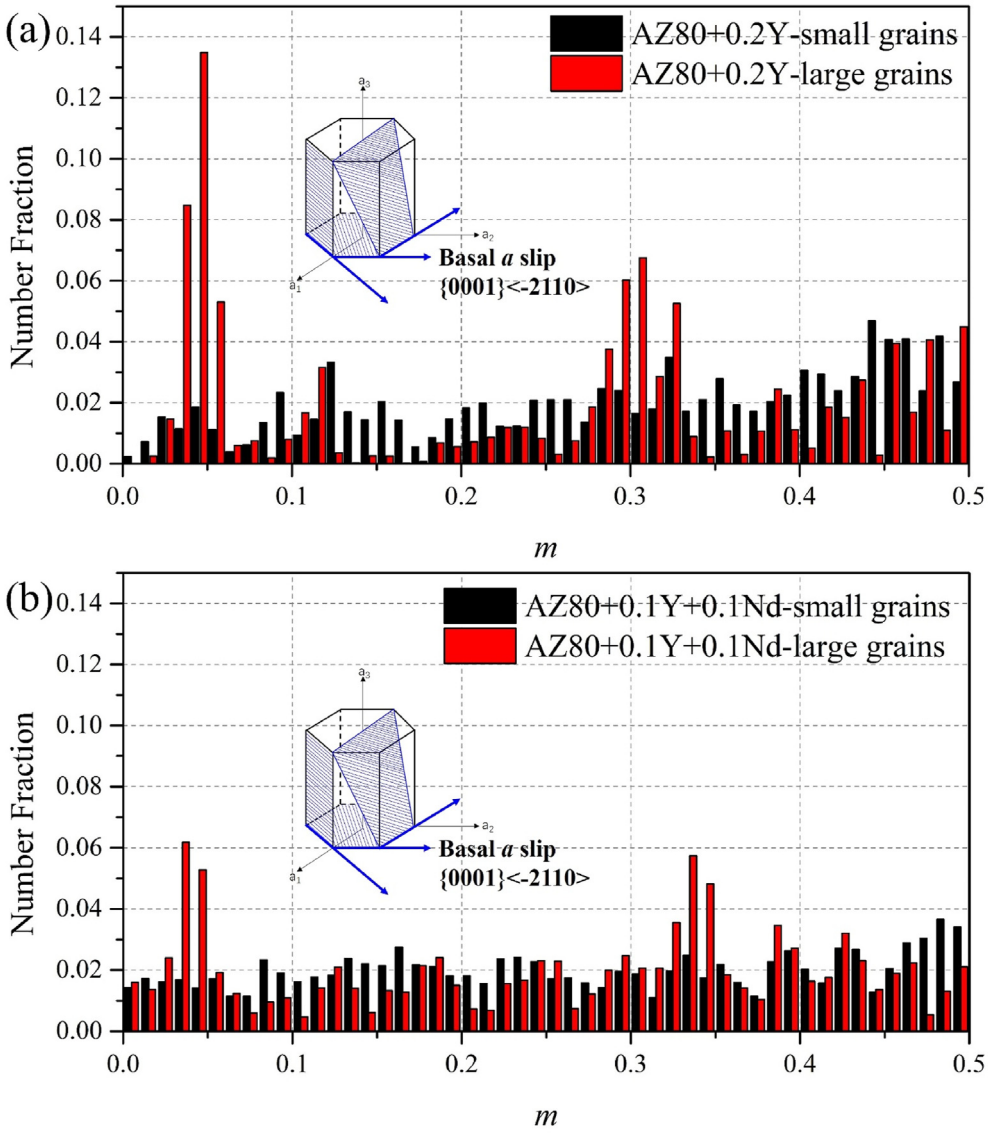

Fig. 9. Schmid factor, *m*, distribution for {0001}<-2110> basal <*a*> slip along ED in the large grains and small grains in the 410 °C/480 h annealed (a) AZ80 + 0.2Y and (b) AZ80 + 0.1Y+0.1Nd. The large and small grains were consistent with the EBSD results in Fig. 8.

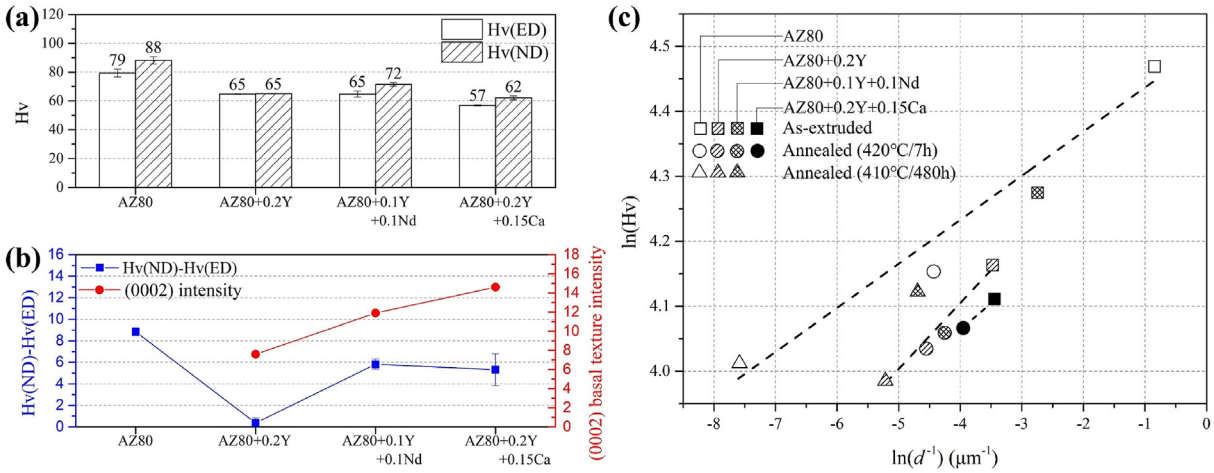

Fig. 10. (a) Vickers hardness comparison between ED and ND for the as-extruded sheets; (b) Vickers hardness difference between ED and ND and the (0002) basal texture intensity for each of the extruded sheets; (c) Variation in Vickers hardness in ND with d^{-1} after different processing conditions.

combination of abundant LAGB and enhanced (0002) basal texture in AZ80 + 0.2Y+0.15Ca favored the lowest grain growth velocity (see Fig. 3) and narrower grain size distribution (low standard deviation of grain size in Table 3). Zeng et al. [18] reported that the co-segregation of (Zn + Ca) to GBs is more effective to reduce the GB energy and enhance the solute drag effect than sole Zn or Ca additions which resulted in more uniform grain growth and a lower migration rate. In the present study, the dual (Y + Ca) was superior to sole Y addition in lowering the grain growth of the AZ80 base alloy, and future work will concentrate on the effort to clarify if can be attributed to the similar (Zn + Ca) GB co-segregation effect. After 420 °C/7 h annealing, the larger grains, which have a larger grain size than the average grain size, exhibited stronger (0002) basal textures than the small grains. For example, Fig. 7 compares the basal texture of big or small grains in 420 °C/7 h annealed AZ80 + 0.2Y (Fig. 7(a and b)) and AZ80 + 0.1Y+0.1Nd (Fig. 7(c and d)). Both alloys exhibited random <0001> pole distributions and weak texture density in the small grains, while more <0001> poles in the larger grains of AZ80 + 0.2Y and AZ80 + 0.1Y+0.1Nd tilted toward ED and ND, respectively, which appeared to cause the texture enhancement [18].

To determine the effect of long-term annealing on the recrystallized grain growth and texture, 410 °C for 480 h (20 days) annealed samples were investigated and compared. Fig. 8(a) shows that the abnormal grain growth was prevalent in AZ80 and the average grain size increased to approximately 2000 μm. Similar to that shown in Fig. 7, characterization was performed on the long-term annealed AZ80 + 0.2Y and AZ80 + 0.1Y+0.1Nd alloys. Both alloys show that the <0001> poles tilt away from ND and extended toward the ED, which indicates the RE texture disappeared after the long-term annealing. Meanwhile, there was a significant difference in the texture between the smaller and the larger grains. For the AZ80 + 0.2Y, less <0001> poles tilted away from the ND and extended toward the ED in smaller grains (Fig. 8 (d)), while the larger grains contained considerable ED oriented <0001> poles (Fig. 8 (e)). Similar texture differentiation was also observed in AZ80 + 0.1Y+0.1Nd (Fig. 8(g and h)), but less difference in texture intensity between the smaller and larger grains was exhibited compared to that for AZ80 + 0.2Y. Both PFs and the texture component distribution indicated that there was more grain growth of some special orientations (e.g., toward ED) after long term annealing, which enhanced the texture and weakened the homogeneity of the grain structure. Similar grain growth was also observed in WE43 alloys after annealing at 545 °C for 840 s [35].

The Schmid factor, m, which serves as one of the typical orientation sensitivity parameters for a given slip system, can be used to illustrate the grain orientation distribution. Fig. 9(a and b) provides the m frequency distribution of the {0001}<-2110> basal <a> dislocation slip along ED for the long-term annealed AZ80 + 0.2Y and AZ80 + 0.1Y+0.1Nd according to Fig. 8(c–f). Both annealed alloys exhibited a relatively random m distribution in the small grains, while a bimodal m distribution was exhibited in the large grain region. For example, the peak positions of m = 0.05, 0.3, and m = 0.05, 0.35 were observed in the larger grain regions for AZ80 + 0.2Y and AZ80 + 0.1Y+0.1Nd, respectively, which implied preferred orientation of the grain growth during SRX. Further, the high m-value peaks may sharpen the basal slip in some large grains, but harden the basal slip when in the low m-value peaks.

3.4. Hardness response to the microstructure evolution

The hardness response varied with the microstructure features (grain size, precipitates, and texture). A comparison of the Vickers hardness results for all the as-extruded sheets in ED and ND is provided in Fig. 10 (a). AZ80 exhibited the highest hardness value in both the ED (79 Hv) and the ND (88 Hv), while AZ80 + 0.2Y+0.15Ca maintained the lowest hardness value. The hardness anisotropy prevalent in the studied alloys has also been reported in previous work [36], and the difference in hardness between ND and ED, Hv(ND)-Hv(ED), is depicted in Fig. 10 (b). The variation trend was similar between hardness difference and (0002) basal texture intensity. This implies the texture strengthening or the hardness sensitivity to crystal orientation plays an important role in the macro-mechanical properties, and the higher (0002) basal texture component introduced more hardness anisotropy (e.g., AZ80 + 0.2Y+0.15Ca).

In addition to the texture, the hardness response varied with the grain size. Generally, there is a positive correlation between the hardness and d^{-n} value [37–40]. Fig. 10 (c) shows that the Vickers hardness (ln(Hv)) increases linearly with ln(d^{-1}) for AZ80 and the microalloyed alloys. AZ80 exhibited higher hardness than that of microalloyed AZ80 at the same grain size. The Al solute depletion (or dilution) in the matrix tend to weak the deformation resistance in Mg–Al series alloys [41,42]. For example, the Al depletion caused by the higher volume fraction of Al–Zr compounds decreases the Al solid solution hardening effects [43]. As a result, the formation of Al_2X (X = Y, Nd, Ca) compounds in the microalloyed AZ80 alloys may result in the decrease of the Al solute strengthening and reduction in hardness. It is noted that the Ca-containing AZ80 alloys exhibited the lowest grain growth velocity and enhanced basal texture, which leads to a finer-grain, textured microstructure. However, the Ca containing sheets maintained the lowest Vickers hardness, which may be related to the modified dislocation slip behavior [44].

4. Conclusions

In this work, Y, (Y + Nd), and (Y + Ca) microalloying effects on the grain growth, texture evolution and the consequent hardness response of AZ80 were investigated during the high-temperature static recrystallization. Some remarks and conclusions are provided as follows:

(1) The microalloying effectively lowered the grain growth rate, in particular, the AZ80 + 0.2Y+0.15Ca maintained the lowest growth rate (231 μm^2/h), which was less than one quarter that of the AZ80 (1020 μm^2/h). Quasi-in-situ EBSD results revealed that the grain boundary migration and grain rotation simultaneously occurred during the grain growth.
(2) The rare-earth (RE) texture components temporarily formed in AZ80 + 0.2Y and AZ80 + 0.1Y+0.1Nd which weakened their basal texture intensity. More <0001> poles of larger grains preferably tilted away from the normal direction and extended toward the extrusion direction resulting in bimodal Schmid factor distributions. In contrast, continuously enhanced basal texture accompanied by grain growth dominated the texture evolution in AZ80 + 0.2Y+0.15Ca.
(3) The microalloying, and especially the Y sole addition, reduced the hardness anisotropy. All the microalloyed alloys exhibited lower Vickers hardness than that of AZ80 for the same grain size. Ca containing microalloyed sheets maintained both the lowest Vickers hardness and a fine-grain, textured structure, which may be related to the modified dislocation slip behavior induced by Ca addition.

Data availability

The raw data required to reproduce these findings cannot be shared at this time as the data also forms part of an ongoing study.

Declaration of competing interest

The authors declare that they have no known competing financial interests or personal relationships that could have appeared to influence the work reported in this paper.

CRediT authorship contribution statement

Lingbao Ren: Investigation, Writing - original draft, Writing - review & editing. **Mingyang Zhou:** Investigation, Writing - review & editing. **Carl J. Boehlert:** Supervision, Writing - review & editing. **Gaofeng Quan:** Project administration, Writing - review & editing.

Acknowledgments

This work was supported by the China Scholarship Council (201707000086). Acknowledgments are given to the 2015 Cultivation Program for the Excellent Doctoral Dissertation of Southwest Jiaotong University (received by Lingbao Ren), the Program of the 2015 Doctoral Innovation Fund of Southwest Jiaotong University (received by Lingbao Ren), and Litmat Technology Chengdu Co., Ltd.

References

[1] H. Huang, G.Y. Yuan, C.L. Chen, W.J. Ding, Z.C. Wang, Excellent mechanical properties of an ultrafine-grained quasicrystalline strengthened magnesium alloy with multi-modal microstructure, Mater. Lett. 107 (2013) 181–184.
[2] T. Homma, N. Kunito, S. Kamado, Fabrication of extraordinary high-strength magnesium alloy by hot extrusion, Scripta Mater. 61 (2009) 644–647.
[3] X.Y. Li, K. Lu, Playing with defects in metals, Nat. Mater. 16 (2017) 700–701.
[4] Z.T. Li, X.D. Zhang, M.Y. Zheng, X.G. Qiao, K. Wu, C. Xu, S. Kamado, Effect of Ca/Al ratio on microstructure and mechanical properties of Mg-Al-Ca-Mn alloys, Mater. Sci. Eng., A 682 (2017) 423–432.
[5] I. Dey, S. Chandra, R. Saha, S.K. Ghosh, Effect of Nb micro-alloying on microstructure and properties of thermo-mechanically processed high carbon pearlitic steel, Mater. Char. 140 (2018) 45–54.
[6] Q. Yang, F.Q. Bu, T. Zheng, F.Z. Meng, X.J. Liu, D.P. Zhang, X. Qiu, J. Meng, Influence of trace Sr additions on the microstructures and the mechanical properties of Mg-Al-La-based alloy, Mater. Sci. Eng., A 619 (2014) 256–264.
[7] Y.B. Hu, C. Zhang, W.Q. Meng, F.S. Pan, J.P. Zhou, Microstructure, mechanical and corrosion properties of Mg-4Al-2Sn-xY-0.4Mn alloys, J. Alloys Compd. 727 (2017) 491–500.
[8] Z. Hu, Q. Hua, H. Yan, X.P. Jie, Y.S. Rao, Effect of trace Sm addition on microstructure and mechanical properties of AZ61 magnesium alloys, Rare Met. Mater. Eng. 45 (2016) 2275–2281.
[9] L.B. Ren, M.Y. Zhou, Y.W.X. Zhang, G.F. Quan, C.J. Boehlert, Effect of 0.4 wt.% yttrium addition and heat treatment on the high-temperature compression behavior of cast AZ80, J. Mater. Sci. 54 (2019) 5757–5772.
[10] F.Q. Bu, Q. Yang, K. Guan, X. Qiu, D.P. Zhang, W. Sun, T. Zheng, X.P. Cui, S.C. Sun, Z.M. Tang, X.J. Liu, J. Meng, Study on the mutual effect of La and Gd on microstructure and mechanical properties of Mg-Al-Zn extruded alloy, J. Alloys Compd. 688 (2016) 1241–1250.
[11] Y. Go, S.M. Jo, S.H. Park, H.S. Kim, B.S. You, Y.M. Kim, Microstructure and mechanical properties of non-flammable Mg-8Al-0.3Zn-0.1Mn-0.3Ca-0.2Y alloy subjected to low-temperature, low-speed extrusion, J. Alloys Compd. 739 (2018) 69–76.
[12] L.B. Ren, G.F. Quan, C.J. Boehlert, Mechanical asymmetry and anisotropy resulting from yttrium addition to AZ80, Mater. Sci. Eng., A, 2020. In preparation.
[13] P. Kumar, A.K. Mondal, S.G. Chowdhury, G. Krishna, A.K. Ray, Influence of additions of Sb and/or Sr on microstructure and tensile creep behaviour of squeeze-cast AZ91D Mg alloy, Mater. Sci. Eng., A 683 (2017) 37–45.
[14] X.J. Zhao, H.W. Chen, N. Wilson, Q. Liu, J.F. Nie, Direct observation and impact of co-segregated atoms in magnesium having multiple alloying elements, Nat. Commun. 10 (2019) 3243.
[15] J.F. Nie, Y.M. Zhu, J.Z. Liu, X.Y. Fang, Periodic segregation of solute atoms in fully coherent twin boundaries, Science 340 (2013) 957–960.
[16] A. Kula, X. Jia, R.K. Mishra, M. Niewczas, Flow stress and work hardening of Mg-Y alloys, Int. J. Plast. 92 (2017) 96–121.
[17] D.A. Basha, H. Somekawa, A. Singh, Crack propagation along grain boundaries and twins in Mg and Mg-0.3 at.%Y alloy during in-situ straining in transmission electron microscope, Scripta Mater. 142 (2018) 50–54.
[18] Z.R. Zeng, Y.M. Zhu, S.W. Xu, M.Z. Bian, C.H.J. Davies, N. Birbilis, J.F. Nie, Texture evolution during static recrystallization of cold-rolled magnesium alloys, Acta Mater. 105 (2016) 479–494.
[19] N. Stanford, M.R. Barnett, The origin of “rare earth” texture development in extruded Mg-based alloys and its effect on tensile ductility, Mater. Sci. Eng., A 496 (2008) 399–408.
[20] L.W.F. Mackenzie, M.O. Pekguleryuz, The recrystallization and texture of magnesium-zinc-cerium alloys, Scripta Mater. 59 (2008) 665–668.
[21] X. Huang, K. Suzuki, Y. Chino, Static recrystallization behavior of hot-rolled Mg-Zn-Ce magnesium alloy sheet, J. Alloys Compd. 724 (2017) 981–990.
[22] I.H. Jung, M. Sanjari, J. Kim, S. Yue, Role of RE in the deformation and recrystallization of Mg alloy and a new alloy design concept for Mg-RE alloys, Scripta Mater. 102 (2015) 1–6.
[23] C.D. Barrett, A. Imandoust, H. El Kadiri, The effect of rare earth element segregation on grain boundary energy and mobility in magnesium and ensuing texture weakening, Scripta Mater. 146 (2018) 46–50.
[24] B. Langelier, A. Korinek, P. Donnadieu, S. Esmaeili, Improving precipitation hardening behavior of Mg-Zn based alloys with Ce-Ca microalloying additions, Mater. Char. 120 (2016) 18–29.
[25] A. Suzuki, N.D. Saddock, J.W. Jones, T.M. Pollock, Solidification paths and eutectic intermetallic phases in Mg-Al-Ca ternary alloys, Acta Mater. 53 (2005) 2823–2834.
[26] S.M. Baek, J.S. Kang, H.J. Shin, C.D. Yim, B.S. You, H.Y. Ha, S.S. Park, Role of alloyed Y in improving the corrosion resistance of extruded Mg-Al-Ca-based alloy, Corros. Sci. 118 (2017) 227–232.
[27] J. Wang, J. Fu, X. Dong, Y. Yang, Microstructure and mechanical properties of as-cast Mg-Al-Sn-Y-Nd alloy, Mater. Des. 36 (2012) 432–437.
[28] Y. Zhong, J. Liu, R.A. Witt, Y. ho Sohn, Z.K. Liu, Al_2(Mg,Ca) phases in Mg-Al-Ca ternary system: first-principles prediction and experimental identification, Scripta Mater. 55 (2006) 573–576.
[29] M. Torabi Parizi, A. Habibolahzadeh, G.R. Ebrahimi, H.R. Ezatpour, Achieving extraordinary combination of strength and elongation of AZ80-0.5Ca alloy, Mater. Sci. Eng., A 690 (2017) 313–322.
[30] J.E. Burke, D. Turnbull, Recrystallization and grain growth, Prog. Met. Phys. 3 (1952) 220–292.
[31] L. Priester, Grain Boundaries and Crystalline Plasticity, John Wiley & Sons, Inc, Hoboken, NJ, USA, 2011.
[32] C.L. Mendis, K. Oh-Ishi, K. Hono, Microalloying effect on the precipitation processes of Mg-Ca alloys, Metall. Mater. Trans. A Phys. Metall. Mater. Sci. 43 (2012) 3978–3987.
[33] L. Wang, T. Xin, D. Kong, X. Shu, Y. Chen, H. Zhou, J. Teng, Z. Zhang, J. Zou, X. Han, In situ observation of stress-induced grain boundary migration in nanocrystalline gold, Scripta Mater. 134 (2017) 95–99.
[34] J.J. Bhattacharyya, S.R. Agnew, G. Muralidharan, Texture enhancement during grain growth of magnesium alloy AZ31B, Acta Mater. 86 (2015) 80–94.
[35] D. Guan, W.M. Rainforth, J. Gao, L. Ma, B. Wynne, Individual effect of recrystallisation nucleation sites on texture weakening in a magnesium alloy: Part 2- shear bands, Acta Mater. 145 (2018) 399–412.
[36] L.B. Ren, G.F. Quan, M.Y. Zhou, Y.Y. Guo, Z.Z. Jiang, Q. Tang, Effect of Y addition on the aging hardening behavior and precipitation evolution of extruded Mg-Al-Zn alloys, Mater. Sci. Eng., A 690 (2017) 195–207.
[37] E.O. Hall, Variation of hardness of metals with grain size, Nature 173 (1954) 948–949.
[38] J. Favre, D. Fabrègue, E. Maire, A. Chiba, Grain growth and static recrystallization kinetics in Co-20Cr-15W-10Ni (L-605) cobalt-base superalloy, Philos. Mag. A 94 (2014) 1992–2008.
[39] P. Bazarnik, Y. Huang, M. Lewandowska, T.G. Langdon, Structural impact on the Hall-Petch relationship in an Al-5Mg alloy processed by high-pressure torsion, Mater. Sci. Eng., A 626 (2015) 9–15.
[40] G.H. Huang, D.D. Yin, J.W. Lu, H. Zhou, Y. Zeng, G.F. Quan, Q.D. Wang, Microstructure, texture and mechanical properties evolution of extruded fine-grained Mg-Y sheets during annealing, Mater. Sci. Eng., A 720 (2018) 24–35.
[41] L.B. Ren, M.Y. Zhou, T.H. Lu, L.L. Fan, Y.Y. Guo, Y.W.X. Zhang, C.J. Boehlert, G.F. Quan, Eutectic phase strengthening and strain rate sensitivity behavior of AZ80 magnesium alloy, Mater. Sci. Eng., A 770 (2020), 138548.
[42] F. Kabirian, R. Mahmudi, Solid solution hardening effect of aluminum on the creep deformation of AZ91 magnesium alloy, Mag. Tech. (2012) 423–426.
[43] R. Mahmudi, S. Moeendarbari, Effects of Sn additions on the microstructure and impression creep behavior of AZ91 magnesium alloy, Mater. Sci. Eng., A 566 (2013) 30–39.
[44] G.M. Zhu, L.Y. Wang, H. Zhou, J.H. Wang, Y. Shen, P. Tu, H. Zhu, W. Liu, P.P. Jin, X.Q. Zeng, Improving ductility of a Mg alloy via non-basal <a> slip induced by Ca addition, Int. J. Plast. 120 (2019) 164–179.